3. Numerical Simulation of Urban Coastal Zones

Yukio Koibuchi and Shinji Sato

3.1 Numerical Modeling in Urban Coastal Zones

Numerical modeling is an essential technique for the understanding and management of water quality in urban coastal zones. This may be because urban coastal zones are characterized by an extremely wide variety of environments with complicated geographical features, such as urban areas that intersect with outer oceans, and hence are affected by both. The phenomena in this area are not only physical, but also biological or chemical, and they interfere with each other. Therefore, the ecosystem and the water quality of urban coastal zones are highly complicated.

The quality of water has long been deteriorating at many of the world's urban coastal zones (Walker 1990). Damage caused by events such as red tides, harmful algal bloom, and decreased amounts of dissolved oxygen in bottom water occur frequently. Such phenomena induce the degradation of aquatic ecosystems and the loss of aquatic resources such as sea grass beds, as well as fish and shellfish. These phenomena – caused by an excessive inflow of nutrients that has been accelerated by urban populations, resulting in the increase of concentrations called eutrophication (Caperon et al. 1971) – have been causing many problems for fisheries and recreation areas in urban coastal zones. However, these events are also influenced by weather conditions, ocean currents, household and industrial wastes, nutrients coming from agricultural lands, sewage treatment plants, acid rain and other such phenomena (Ærtebjerg et al. 2003). Furthermore, the interactions between all of these factors are quite complicated. Actually, distinguishing between natural and anthropogenic effects is not easy (Jøgensen and Richardson 1996). This makes the improvement of water quality and the management of resources in this area even more difficult.

H. Furumai et al. (eds.), *Advanced Monitoring and Numerical Analysis of Coastal Water and Urban Air Environment*,

Numerical modeling that deals quantitatively with these complex systems has been in development since the 1960s, much like digital computers. The use of modeling also has important practical applications, such as the prediction and management of water quality and ecosystems in urban coastal zone.

This chapter describes how water quality and pathogens are modeled in urban coastal areas. Sect. 3.1.2 explains the basic structure of these models. Physical and ecosystem modeling techniques for enclosed bays are described in Sect. 3.1.3. Sect. 3.1.4 shows the application of ecosystem modeling as a tool for integrated management.

Next, Sect. 3.2 describes pathogen modeling in urban coastal areas.

3.1.1 Introduction to Physical Numerical Modeling in Urban Coastal Areas

Water quality is directly and indirectly influenced by a variety of flows. For example, since phytoplankton drifts passively according to water flows, it is strongly influenced by the distribution of the flow of the bay (Lucas et al. 1999). Bay water motions also exert a strong influence on other water quality parameters. These kinds of influences are direct and obvious. The degree of influence naturally increases with the strength of the currents.

In contrast, even if the flow is very small, it has some spatial patterns in common with outer bay directions. In this case, a nutrient load that is discharged at the head of the bay is transported to distant locations and, probably, the water exchange rate of the bay also increases. The nutrient loading that is permissible – i.e. which the bay can accept – will then increase due to the increase in the water exchange rate. For water retention rates, the strength of currents is not as important as spatial patterns. For example, tidal currents are dominant in urban coastal areas. However they are oscillatory. Water particles in tidal currents move to the head of the bay during flood tides, but move back to the mouth of the bay during ebb tides. As a result, tidal currents do not substantially transport water particles. In contrast, density currents are clearly weaker than tidal currents, but they flow in one direction continuously and transport water particles more efficiently. As a result, they substantially effect water retention times and ecosystem characteristics.

A water quality model for bays must therefore consist of a three-dimensional circulation model and an ecosystem model that describes

pelagic and benthic aspect of nutrients cycling. This section focuses on the physical modeling and the next section deals with water quality modeling. The final section discusses the application of these models to Tokyo Bay.

3.1.2 Three-Dimensional Hydrodynamic Model

Many three-dimensional hydrodynamic models have been developed in the last decades, including POM (Princeton Ocean Model; Blumberg and Mellor 1987), CH3D (Curvilinear Hydrodynamics in 3 Dimensions; Johnson et al. 1993) and ROMS (Regional Ocean Modeling System; MacCready et al. 2002; Li et al. 2005). These models solve the Navier-Stokes equation with the forcing (the wind stress, Coriolis force and buoyancy force) under adequate approximations that are called the hydrostatic and Boussinesq approximations.

Hydrostatic approximation assumes that there is a perfect balance between pressure gradients and gravity: in other words, no acceleration occurs in a vertical direction. This is justified because the aspect ratio of urban coastal areas is extremely small, and hence the vertical motions are considered to be small and also to be further inhibited by gravitational forces under stable density stratification. This means that vertical acceleration is negligible and the fluid behaves as though it were under static equilibrium as far as vertical motion is concerned (Prudman 1953).

Density variations in urban coastal areas are also small (less than 3% or so), and so density can be considered to be constant, except when body forces resulting from the motion of a density stratified fluid in a gravitational field are concerned. This approximation is called the Boussinesq approximation: in other words, changes in the mass or inertia of a fluid body due to the changes in its density are negligible, while the same changes in density are consequential when the gravitational field is present (Kantha and Clayson 2000). Therefore, following Boussinesq (1903), this approximation justifies replacing ρ by a constant reference density ρ_0 everywhere except in terms involving gravitational acceleration constant g. Under such approximations, the governing equations are transformed as follows:

$$\frac{\partial u}{\partial t}+u\frac{\partial u}{\partial x}+v\frac{\partial u}{\partial y}+w\frac{\partial u}{\partial z}$$
$$=fv-g\frac{\partial \eta}{\partial x}-\frac{g}{\rho_0}\frac{\partial}{\partial x}\int_z^\eta \rho' g dz+\frac{\partial}{\partial x}(A_x\frac{\partial u}{\partial x})+\frac{\partial}{\partial y}(A_y\frac{\partial u}{\partial y})+\frac{\partial}{\partial z}(A_z\frac{\partial u}{\partial z}) \quad (3.1)$$

$$\frac{\partial v}{\partial t}+u\frac{\partial v}{\partial x}+v\frac{\partial v}{\partial y}+w\frac{\partial v}{\partial z} \tag{3.2}$$
$$=fu-g\frac{\partial \eta}{\partial y}-\frac{g}{\rho_0}\frac{\partial}{\partial y}\int_z^\eta \rho' g dz+\frac{\partial}{\partial x}(A_x\frac{\partial v}{\partial x})+\frac{\partial}{\partial y}(A_y\frac{\partial v}{\partial y})+\frac{\partial}{\partial z}(A_z\frac{\partial v}{\partial z})$$

$$\frac{\partial u}{\partial x}+\frac{\partial v}{\partial y}+\frac{\partial w}{\partial z}=0 \tag{3.3}$$

Here, t stands for time. u, v, and w are the velocity components in x, y, and z directions. The symbol ρ' is the reference density and it is defined as $\rho = \rho_0 + \rho'$. The symbols A_x, A_y and A_z are the eddy viscosities in x, y, and z directions. The symbol g is the acceleration due to gravity.

3.1.2.1 Grid Systems of Urban Costal Model

All currents including tides, wind-driven currents, and density currents in urban coastal zones are strongly influenced by geometry and bathymetry, whereas these areas are rarely regular in shape. In particular, a coastline near an urban coastal area is more complex, due to reclamations and the constructions of harbors, than a natural one. In addition, the uniformity of the bathymetry further lessened as a result of dredging for vessel transport. A computational grid is required to accurately represent such complex geometry and bathymetry. For this reason, the selection of which grid system to use has varied along with the progress of modeling, although the governing equations are not basically different.

For vertical coordinate systems (shown in Fig. 3-1), Cartesian (z-coordinate vertical grid) and sigma-coordinate grids have been widely used. A Cartesian grid is easy to understand, and shows the correspondence between program codes and governing equations. It is sometimes more accurate than sigma-coordinate grids, especially if the bathymetry of the bay is simple and mild. The sigma-coordinate system tends to have an error featuring the presence of steep-bottom topography. However, unless an excessively large number of vertical levels are employed, the Cartesian grid fails to represent the bottom topography with satisfied accuracy.

The sigma-coordinate system is convenient in the sense that it can essentially introduce a "flattening out" mechanism for variable bottoms at z = −h(x, y). The flow near the seabed is also calculated well. Moreover, the sigma-coordinate system is easy to program since the number of vertical grids can be the same, and the setting of boundary conditions will be simple. The sigma-coordinate system has long been widely used in both meteorology and oceanography (Phillips 1957; Freeman et al. 1972).

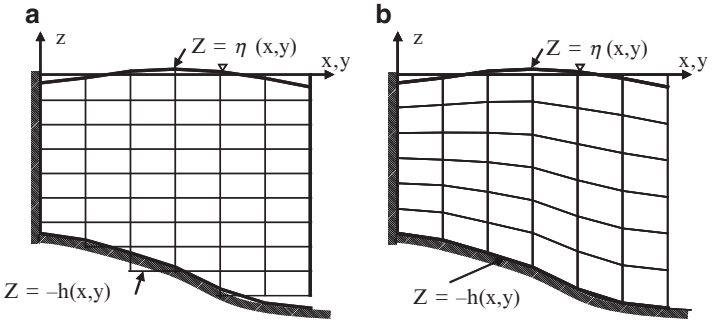

Fig. 3-1. Examples of two vertical grid systems: (**a**) a Cartesian or *z*-coordinate vertical grid and (**b**) a sigma-coordinate vertical grid system

After the incorporation of approximations, the governing equations in the sigma coordinate system are as follows:

$$\frac{\partial(Hu)}{\partial t}+\frac{\partial(Huu)}{\partial x}+\frac{\partial(Hvu)}{\partial y}+\frac{\partial(H\dot{\sigma}u)}{\partial \sigma} = Hfv-\frac{H}{\rho}\frac{\partial p}{\partial x}+\frac{1}{H}\frac{\partial}{\partial \sigma}(A_v\frac{\partial u}{\partial \sigma})+HA_h\left(\frac{\partial^2 u}{\partial x^2}+\frac{\partial^2 u}{\partial y^2}\right) \tag{3.4}$$

$$\frac{\partial(Hv)}{\partial t}+\frac{\partial(Huv)}{\partial x}+\frac{\partial(Hvv)}{\partial y}+\frac{\partial(H\dot{\sigma}v)}{\partial \sigma} = Hf(-u)-\frac{H}{\rho}\frac{\partial p}{\partial y}+\frac{1}{H}\frac{\partial}{\partial \sigma}(A_v\frac{\partial v}{\partial \sigma})+HA_h\left(\frac{\partial^2 v}{\partial x^2}+\frac{\partial^2 v}{\partial y^2}\right) \tag{3.5}$$

$$-\frac{1}{\rho}\nabla p=-\frac{1}{\rho}\left[\left(\rho_0+\rho'\sigma\right)g\nabla_\sigma\eta+\rho' g(\sigma-1)\nabla_\sigma h+\nabla_\sigma\left[H\int_\sigma^1\rho' g d\sigma\right]\right] \tag{3.6}$$

$$\sigma=\frac{z+h}{h+\eta} \tag{3.7}$$

$$\dot{\sigma}=\frac{\partial\sigma}{\partial t}+u\frac{\partial\sigma}{\partial x}+v\frac{\partial\sigma}{\partial y}+w\frac{\partial\sigma}{\partial z} \tag{3.8}$$

where, t stands for time. u, v, and $\dot{\sigma}$ are the velocity components in x, y, and z directions in the $\dot{\sigma}$ coordinate system. η is change in surface elevation, h is initial water depth, and H is the total water depth ($H=h+\eta$). f is the Coriolis coefficient and P stands for pressure. ρ and ρ' are the constant reference density and the deviation from it, and $\rho = \rho_0 + \rho'$. $A_H$and A_V are the horizontal and vertical eddy viscosity coefficients, respectively. g is acceleration due to gravity.

Recently, the stretched grid system (S-grid system) has also been popular. This grid system is an extension of sigma-coordinate system. Generally, a sigma-coordinate grid divides the vertical coordinate into an equal number of points. The S-grid system has a higher resolution near the surface and bottom (Haidvogel et al. 2000).

Wind-stress and bottom friction are considered at surface and bottom boundary conditions, respectively. Settings in boundary conditions are easy in sigma-coordinate systems since they use the same number of vertical grids. At lateral boundaries, normal velocities are set at zero, and a free slip condition is applied to the friction terms. At open boundary, the velocity gradient is set at zero.

Horizontal computational grids are also modified to fit topography. The simplest horizontal computational grid is the rectangular grid with fixed spacing. The rectangular grid is equivalent to the Cartesian vertical grid. Recently, curvilinear coordinate systems have been widely used. These systems allow greater flexibility than rectangular grid systems. Fig. 3-2 is

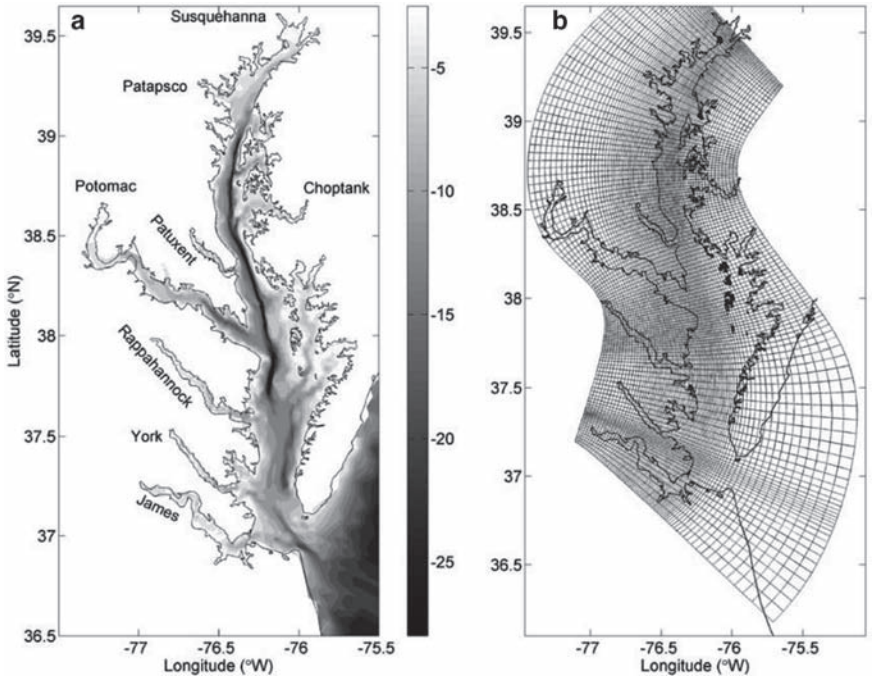

Fig. 3-2. Examples of curvilinear horizontal coordinate systems. (**a**) Bathymetry of the Chesapeake Bay and its adjacent coastal area. Depths are in meters. (**b**) A horizontal curvilinear coordinate system designed for resolving the bay's complex coastlines and deep channel (from Ming et al. 2005)

an example of a horizontal curvilinear coordinate system. The Chesapeake Bay, like other bays, has a typical complex geometry, and thus a horizontal curvilinear coordinate system is advantageous (Li et al. 2005).

This is extended to a nested grid system in which finer grids are used in regions to yield detailed information.

3.1.2.2 Density Effect Modeling for Urban Coastal Waters

In urban coastal areas, density difference plays an essential role for water quality and currents. One of the most important phenomena induced by the density effect is stratification. Once stratification occurs in a coastal zone, surface water and bottom water are isolated. This process is very important when we discuss the distributions of pollutants from the land. Stratification also enhances the increase of phytoplankton in the surface layer and oxygen depletion near the seabed. Moreover, estuarine circulation is induced by density differences in the salty sea water and the river flow. Fig. 3-3 shows a schematic diagram of estuarine circulation. River water runs through the urban area and runs off from the river mouth, spreading over the sea surface like a veil since river water has low density compared with saline sea water. To cancel the density difference between the river water and the saline water, a great deal of sea water is entrained into the river water flow. Such a mixing process continues until the river water reaches the same density as the surrounding sea water, resulting in vertical circulation in the bays that is is several to ten times greater than the river flux (Unoki 1998). Thus, estuarine circulation induces seaward currents on the surface and landward currents near the bottom. The speed of the currents is slow compared with the tidal currents, as explained previously. Since estuarine circulations are in a fixed direction, its material transport is very effective over a long time scale in spite of the small magnitude of its velocity.

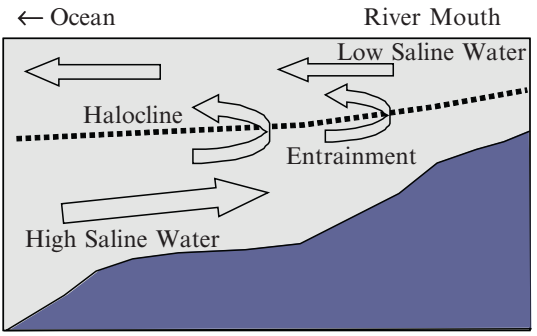

Fig. 3-3. Cross-sectional view of two-layer estuarine circulation in a bay

Estuarine circulation also plays an important role in the nutrient cycles of stratified bays. Organic matters are deposited on the seabed after phytoplankton blooms or river runoffs. They are decomposed by bacteria in the seabed. These nutrients are supplied from the seabed under anoxic condition in summer.

In order to include density effects in the numerical model, conservation equations for temperature and salinity are also included. Then, to obtain a realistic prediction for vertical stratification, a turbulent closure model is employed (Mellor and Yamada 1982). Consequently, flows driven by various mechanisms – e.g. the gravitational, wind-driven, and topographically induced flows – can be reproduced within physical numerical models.

Diffusion equations for temperature and salinity in the sigma coordinate system are as follows:

$$\frac{\partial(HT)}{\partial t}+\frac{\partial(uHT)}{\partial x}+\frac{\partial(vHT)}{\partial y}+\frac{\partial(\dot{\sigma}HT)}{\partial \sigma}= \tag{3.9}$$
$$HK_H\left(\frac{\partial^2 T}{\partial x^2}+\frac{\partial^2 T}{\partial y^2}\right)+\frac{1}{H^2}\frac{\partial}{\partial \sigma}\left(K_V\frac{\partial HT}{\partial \sigma}\right)+\frac{1}{\rho C_P}\frac{dQ(\sigma)}{d\sigma}$$

$$\frac{\partial(HS)}{\partial t}+\frac{\partial(uHS)}{\partial x}+\frac{\partial(vHS)}{\partial y}+\frac{\partial(\dot{\sigma}HS)}{\partial \sigma}= \tag{3.10}$$
$$HK_H\left(\frac{\partial^2 S}{\partial x^2}+\frac{\partial^2 S}{\partial y^2}\right)+\frac{1}{H^2}\frac{\partial}{\partial \sigma}\left(K_V\frac{\partial HS}{\partial \sigma}\right)-RS$$

Here, T and S stand for temperature and salinity, respectively. Heat balance and moisture balance at surface are considered as surface boundary condition for temperature and salinity, respectively. C_P and Q stands for specific heat coefficient and net surface heat flux at the surface, respectively. R stands for river discharge. k_H and k_V are the horizontal and vertical eddy diffusion coefficients, respectively.

3.1.2.3 Turbulence Closure

The vertical mixing coefficients, V_A and V_K are obtained by appealing to the second order turbulent closure scheme of Mellor and Yamada (1982), which characterizes turbulence by equations for the kinetic energy of turbulence, q^2, and turbulence macro scale l, according to:

$$\frac{Dq^2}{Dt}=K_q\frac{\partial q^2}{\partial z}+aA_v\left[\left(\frac{\partial u}{\partial z}\right)^2+\left(\frac{\partial v}{\partial z}\right)^2\right] \tag{3.11}$$
$$+\frac{2g}{\rho_0}K_V\frac{\partial \rho}{\partial z}-\frac{2q^3}{B_1 l}+A_H\frac{\partial q^2}{\partial^2 x}+A_H\frac{\partial q^2}{\partial^2 y}$$

$$\frac{Dq^2}{Dt} = K_q \frac{\partial q^2}{\partial z} + aA_v \left[\left(\frac{\partial u}{\partial z} \right)^2 + \left(\frac{\partial v}{\partial z} \right)^2 \right] + \frac{2g}{\rho_0} K_V \frac{\partial \rho}{\partial z} - \frac{2q^3}{B_1 l} + A_H \frac{\partial q^2}{\partial^2 x} + A_H \frac{\partial q^2}{\partial^2 y} \tag{3.12}$$

Wall proximity functions $\bar{W}$ is defined as follows:

$$\bar{W} = 1 + E_2 \left(\frac{1}{kL} \right)^2 \tag{3.13}$$

where

$$\frac{1}{L} = \frac{1}{\eta - z} + \frac{1}{H + z} \tag{3.14}$$

Mixing coefficients are given as:

$$A_V = S_M l q \tag{3.15}$$

$$K_V = S_H l q \tag{3.16}$$

$$K_q = S_q l q \tag{3.17}$$

The stability functions S_M, S_H, and S_q are analytically derived from algebraic relations. They are functionally dependent on $\frac{\partial u}{\partial z}, \frac{\partial v}{\partial z}, g\rho_0 \frac{\partial \rho}{\partial z}$, q and l. These relations are derived from closure hypotheses described by Mellor (1973) and later summarized by Mellor and Yamada (1982).

3.1.2.4 Numerical Scheme

A semi-implicit finite difference scheme has been adopted where equations are discretized explicitly in the horizontal direction and implicitly in the vertical direction. An Arakawa C staggered grid has been used with the first order upwind scheme. The tri-diagonal formation of the momentum equation is utilized, and in combination with the mass conservation equation, an algebraic equation is obtained where the only unknown variable is the surface elevation η in implicit form. This algebraic equation is solved through the successive over relaxation (SOR) method.

3.1.3 Ecosystem Modeling of Coastal Regions

The phenomena in urban coastal zone are not only physical but also biological or chemical, each of which relates to the other. The ecosystems and water

quality of urban coastal zones are highly complicated. To deal with these complex systems, a water quality model is composed of a three-dimensional physical circulation model and an ecosystem model that describes pelagic and benthic aspect of nutrients cycling. The pelagic and benthic systems also have interactions with each other.

In ecosystem models, each water quality variable is often called a compartment. Various kinds of models are also proposed for ecosystem models (Kremer and Nixon 1978; Fasham et al. 1990; Chai et al. 2002; Kishi et al. 2007). Some models, such as CE-QUAL-ICM (Cerco and cole 1995), Delft3D-WAQ (delft Hydraulics 2003), MIKE3_WQ [Danish Hydraulic Institute (DHI) 2005], RCA&ECCOM (Hydroqual 2004), etc., have been widely used to simulate water quality in estuaries and in the ocean.

Each model is developed with basic aquatic compartments such as phytoplankton, zooplankton, and nutrients. Some differences in the modeling of sediment, detritus, and the detailed modeling of phytoplankton exist, depending on the target ecosystems and the objectives of the study. As a result, no fully adaptive model applicable for all water bodies exists. If we were to make a model that could be adapted for all areas, its results would be too complex to discuss. It would not be so different from observing the real world. For example, ocean ecosystem models tend to focus only on pelagic systems. They tend to ignore benthic modeling, since the open ocean is deep enough to prevent the return of detritus to the seabed. Meanwhile, ocean ecosystem models generally deal with some metals in order to represent the limiting factor of phytoplankton. These metals are fully abundant in urban coastal zones. However, they are often depleted during phytoplankton growth in the open ocean. On the other hand, the concentration of phytoplankton in coastal areas is highly variable both spatially and temporally as compared to the open sea. Subsequent sedimentation of this bloom also constitutes a major input to benthic ecology (Waite et al. 1992; Matsukawa 1990; Yamaguchi et al. 1991). To represent these phenomena, ecosystem models of coastal zones usually cover benthic systems.

Ecosystem models solve conservation equations for relevant components with appropriate source and sink terms. This is the same as temperature and salinity modeling in physical models, as explained in Sect. 3.1.4.

For the sigma coordinate system, a mathematical formulation of the conservation of mass is written by:

$$\frac{\partial (HC)}{\partial t}+\frac{\partial (uHC)}{\partial x}+\frac{\partial (vHC)}{\partial y}+\frac{\partial (\dot{\sigma} HC)}{\partial \sigma}=$$

$$HK_H\left(\frac{\partial^2 C}{\partial x^2}+\frac{\partial^2 C}{\partial y^2}\right)+\frac{1}{H^2}\frac{\partial}{\partial \sigma}\left(K_V\frac{\partial HC}{\partial \sigma}\right)\pm S(x,y,\sigma,t)+W(x,y,\sigma,t)$$

where C denotes concentration of the water quality variable and t is time. Fluxes into and out of the target control volume are calculated by using physical model results. $S(x,y,\sigma,t)$ represents sources or sinks of the water quality variable due to internal production and the removal of the biogeochemical effect. It also represents the kinetic interactions of each compartment. $W(x,y,\sigma,t)$ represents the external inputs of the variable c.

For example, phytoplankton constitutes the first level in the food chain of the pelagic ecosystem of bays. Phytoplankton photosynthesizes by using sunlight and increases. At this time, the source term S of phytoplankton is increased depending on the amount of photosynthesis that takes place. Phytoplankton is then decreased by the grazing of zooplankton. The source term S of zooplankton is increased along with this grazing, and the source term of phytoplankton is decreased. Ecosystem models basically express the relationship of each compartment through mathematical expressions. These models provide a quantitative description of the influences of physical circulation on the biological and chemical processes of urban coastal zones.

3.1.3.1 Outline of an Ecosystem Model Description

The ecosystem model introduced here was developed to simulate the nutrient budget of an urban coastal zone. It includes the temporal and spatial variations of phytoplankton, nutrients, detritus, and dissolved oxygen (DO). In urban coastal zones, nutrients emitted from urban areas are not a limiting factor for phytoplankton growth. However, quantifying the nutrient budget is essential for analyzing and restoring the ecosystems of urban coastal zones. Fig. 3.4 shows schematic interactions of a lower trophic ecosystem model which is used for Tokyo Bay (Koibuchi et al. 2001) This model has 18 state variables: phytoplankton (Phy), zooplankton (Zoo), nutrients (NH4, NO3, PO4 and Si), labile detritus (LDON, LDOP, LDOSi) and refractory detritus (RDON, RDOP, RDOSi) for each nutrient, labile detritus carbon (LDOC), refractory detritus carbon (RDOC), dissolved organic carbon (DOC), and dissolved oxygen (DO), as well as sedimentation processed from particulate organic material.

Since the basic structure of the model follows the widely applied CE-QUAL-ICM (Cerco and Cole 1993, 1995), this section mainly focuses on our modifications of the CE-QUAL-ICM model in the following description.

3.1.3.2 Phytoplankton and Zooplankton Modeling

This model deals with four phytoplankton groups. Phyd1 is based on *Skeletonema costatum,* which is a dominant phytoplankton species in Tokyo Bay. Phyd2 represent a winter diatom group (such as *Eucampia*).

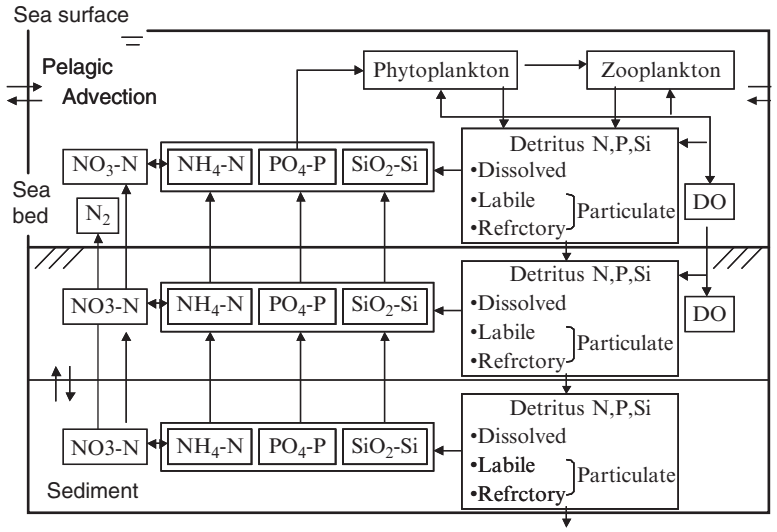

Fig.3-4. Idealized nutrient cycling in Tokyo Bay's ecosystem according to the model of Koibuchi et al. (2001). Cycling between the 18 state variables: phytoplankton, zooplankton, nutrients (nitrogen, phosphorus, and silicate), labile detritus and refractory detritus for each nutrient, and dissolved oxygen, as well as sedimentation processed from particulate organic materials

Phyr is a mixed summer assemblage consisting primarily of *Heterosigma akashiwo* and *Thalassosira*. Phyz denotes the dinoflagellates. These four phytoplankton assemblages have different optimal levels of light for photosynthesis, maximum growth rates, optimal temperatures for growth, and half saturation constants for nutrient uptake. Diatoms only use silica during growth.

The time rate of change of phytoplankton due to biological activity and sink is given by:

$$\frac{\partial Phy_x}{\partial t} = \mu_x Phy_x - gZoo - m_p Phy_x - W_{px}\frac{\partial Phy_x}{\partial z} \tag{3.18}$$

where $x = d1, d2, r, z$, denote each phytoplankton assemblage. The phytoplankton growth rate μ depends on temperature T, on photosynthetically available radiation I, and on the nutrient concentration of nitrogen, phosphorus, and silica :

$$\mu_x = \mu_{\max}(T)\cdot L(I)\cdot Min\left(L_N, L_P, L_{Si}\right) \tag{3.19}$$

$$\mu_{\max}(T) = \mu_{\max} \exp\left[-\beta_1 \left(T_{opt} - T\right)^2\right] \quad T \le T_{opt}, \tag{3.20}$$

or

$$\mu_{\max}(T) = \mu_{\max} \exp\left[-\beta_2 \left(T_{opt} - T\right)^2\right] T > T_{opt},$$

$$L(N) = (L_{NO3} + L_{NH4}) \tag{3.21}$$

$$L_{NO3} = \frac{NO3}{k_{NO3} + NO3} \frac{1}{1 + NH4 / k_{NH4}},$$

$$L_{NH4} = \frac{NH4}{k_{NH4} + NH4},$$

$$L(P) = \frac{PO4}{k_{PO4} + PO4} \tag{3.22}$$

$$L\left(Si\right) = \frac{Si}{k_{Si} + Si} \tag{3.23}$$

where $\mu_{\max}$ (T) is the growth rate at ambient temperature, which relates $\mu_{\max}$, the maximum growth rate $\mu_{\max} = \mu_0 \cdot 1.066^T$ (Eppey 1972), T_{opt}, the optimal temperature of each plankton assemblage, and β_1 and β_2 are shaping coefficients, k_{NO3}, k_{NH4}, k_{PO4} and k_{Si}, which is the Michaelis of the half-saturation constant for each nutrient. I is exponentially decreasing with water depth z according to:

$$I = I(z) = \tag{3.24}$$

$$I_0 \cdot par \cdot \exp\left\{-z\left(K_w + K_{\mathrm{chl}} \int_z^0 Ch(z)dz + K_{\mathrm{Sal}} \frac{1}{H + \eta} \int_z^0 Sal(z)dz\right)\right\}$$

where I_0 is shortwave radiation, and *par* is the fraction of light that is available for photosynthesis. K_w, K_{Chl}, and K_{Sal} are the light attenuation coefficients for water, chlorophyll, and depth average salinity, respectively.

Suspended sediment reduces underwater light intensity and affects the growth of phytoplankton. The effect of suspended sediment concentration on light intensity should be simulated as its own compartment. However, the re-suspension rate of mixed mud and the available data on the concentration of sediment suspended in river water and on the seabed are very limited. Therefore, we used observation results of salinity based on field observation data from 1999 and 2000, as shown in Fig. 3-5.

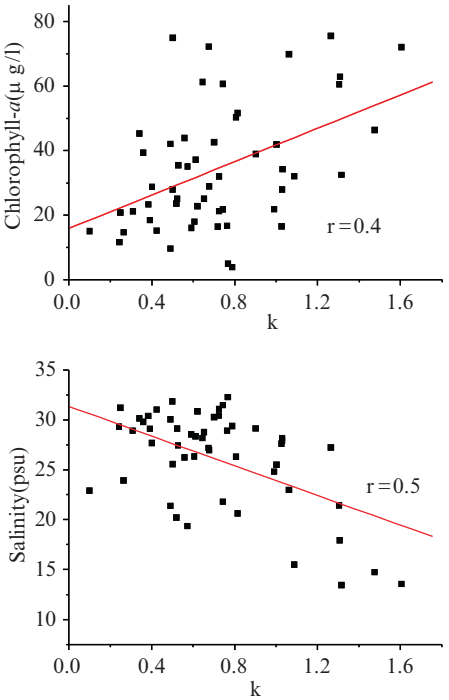

Fig. 3-5. Correlation between light attenuation constant k and Chlorophyll-*a* concentration (*top*), light attenuation constant k and salinity (*bottom*)

The function $L(I)$ represents the photosynthesis–light relationship (Evans and Parslow 1985),

$$L(I) = \frac{\alpha I}{\sqrt{\mu_{\max}^2 + \alpha^2 I^2}} \tag{3.25}$$

The rate of phytoplankton grazing, g, which is a function of an ambient temperature:

$$g = k_{grz}\theta_{grz}^{(T-20)} \tag{3.26}$$

where k_{grz} is the predation rate at 20°C. Other phytoplankton loss terms are mortality, represented by the linear rate m_p, where W_{px} is the constant vertical sinking velocity for each phytoplankton.

The growth rates of zooplankton are expressed as follows:

$$\frac{\partial Zoo}{\partial t} = g\beta Zoo - l_{BM}Zoo - l_E g\beta Zoo - m_Z Zoo^2 \tag{3.27}$$

Here β is the assimilation efficiency of phytoplankton by zooplankton, and l_{BM} and l_E denote excretion due to basal metabolism and ingestion, while the remaining fraction is transferred to the detritus. m_Z is the loss coefficient of zooplankton mortality.

3.1.3.3 Nutrients and Detritus Modeling

The nutrient compartments have four principal forms for each nutrient (nitrogen, phosphorus, and silica): dissolved organic nutrients, labile and refractory particulate organic nutrients (LPON and RPON, respectively), and dissolved inorganic nutrients. Only the dissolved inorganic nutrients are utilized by phytoplankton for growth. Nutrients are changed to these various organic and inorganic forms via respiration and predation. Fig. 3.6 shows an example of nutrient cycles using phosphorus. DOP, LPOP, and RPOP work as a pool of phosphorus.

For example, certain labile compounds that are rapidly degraded, such as the sugars and amino acids in the particulate organic matter deposited on the sediment surface, decompose readily; others, such as cellulose, are more refractory, or resistant to decomposition.

Table 3.1 shows the distributions of each detritus form by each event, based on Pett (1989).

Ammonia and nitrate are utilized by phytoplankton for growth. Ammonia is the preferred form of inorganic nitrogen for algal growth, but phytoplankton utilize nitrate when ammonia concentrations become depleted. Nitrogen is returned from algal biomass to the various dissolved and particulate organic nitrogen pools through respiration and predatory grazing. The time rates for variations due to the biological processes of nitrate and ammonium are as follows. Denitrification does not occur in the pelagic water systems in this model, but rather occurs in the anoxic sediment layer. As a result, if denitrification occurs in the sediment, nitrate is transferred by diffusion effect into the sediment.

$$\frac{\partial NO3}{\partial t} = -\mu_{\max\_X} L(I) L_{NO3} Phy_x + nNH4 \tag{3.28}$$

$$\frac{\partial NH4}{\partial t} = -\mu_{\max\_X} L(I) L_{NH4} Phy_x - nNH4 + l_{BM} Zoo + l_E g \beta Zoo + r_{DON} DON \tag{3.29}$$

Phosphorus kinetics is basically similar to nitrogen kinetics except for the denitrification and the alkaline phosphatase effects of the DOP degradation processes. Many phytoplankton can enhance alkaline phosphatase activity. This effect makes it possible for them to use phosphate from DOP pools

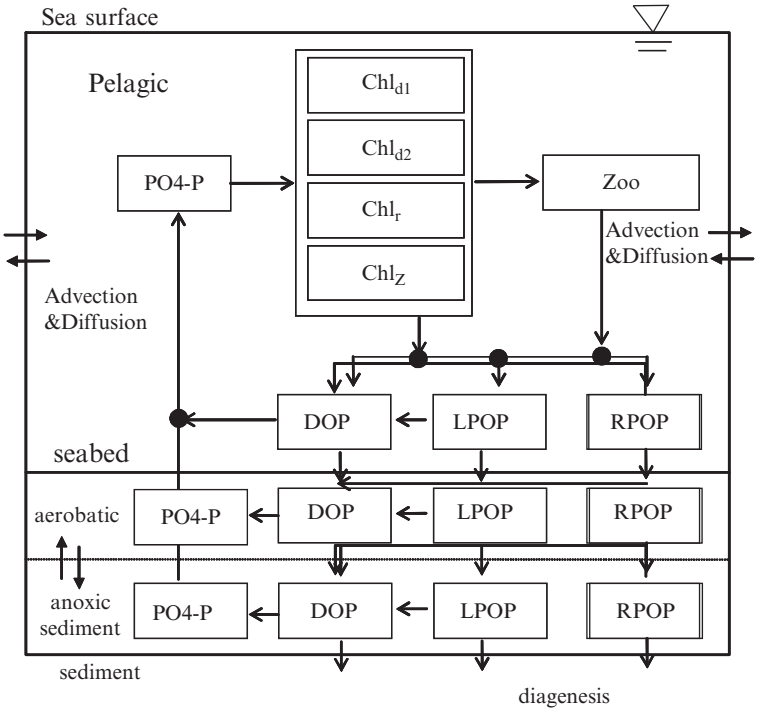

Fig. 3-6. Phosphorus cycles in the model

Table 3-1. Divide ratio of detritus

	Detritus type	asal metabolism	Predation	Mortality of zooplankton
Carbon	*DOC* dissolved organic carbon	1	0.1	0.2
	LPOC labile particulate organic carbon	0		0.45
	RPOC refractory particulate organic carbon	0		0.35
Nitrogen	*DON* dissolved organic nitrogen	1	0.1	0.1
	LPON labile particulate organic nitrogen	0	0	0.45
	RPON refractory particulate organic nitrogen	0	0	0.35
	NH4 ammonia	0	0	0.1
Phosphorus	*DON* dissolved organic phosphorus	1	0.3	0.2
	LPON labile particulate organic phosphorus	0	0	0.35
	RPON refractory particulate organic phosphorus	0	0	0.15
	PO4 phosphate	0	0	0.3

(Fitzgerald and Nelson 1966). This effect is formulated in the following model:

$$\frac{\partial PO4}{\partial t} = -\mu_{\max\_X} L(I) L_{PO4} Phy_x + l_{BM} Zoo + l_E g \beta Zoo + r_{DOP} DOP \tag{3.30}$$

$$r_{DOP} = r_{DOP\_\min} + \frac{k_{PO4}}{k_{PO4} + PO4} r_{DOP\_di} \sum_{X=di1,di2} Chl_x \tag{3.31}$$

where, r_{DOP} is the decomposition rate for DOP, $r_{DOP–\min}$ is the minimum constant of DOP decomposition(day^{-1}), $k_{PO4}$is a half saturation constant of phosphate uptake, and $r_{DOP–di}$is the acceleration effect of DOP decomposition by diatoms.

The kinetics of the silica is fundamentally the same as the kinetics of the phosphorus. Only diatoms utilize silica during growth. Silica is returned to the unavailable silica pool during respiration and predation.

3.1.3.4 Sediment Processes

The sediment system is zoned in two layers (see Fig. 3.6), an aerobic and an anoxic layer. Organic carbon concentrations in the sediment are controlled by detritus burial velocity, the speed of labile and refrigerate organic carbon decomposition, and the rate constant for the diagenesis of particulate organic carbon. The thickness of the aerobic layer is calculated by oxygen diffusion when the amount of oxygen at the bottom layer of the pelagic system isn't zero. The nutrient model, which is a simplified version of the model, treats the nutrients ammonium, nitrate, phosphate, and silica and their exchanges with the pelagic system. Silicate-dependent diatoms and non-silicate-dependent algae are distinguished.

3.1.3.5 Dissolved Oxygen

Dissolved oxygen is an essential index for the water quality of an urban coastal zone. Sources of DO included in the model are reaeration at the sea surface, photosynthesis of phytoplankton, and DO in inflows. The sink of DO includes respiration of phytoplankton and zooplankton, oxidation of detritrial carbon (LDOC and RDOC), nitrification, and sediment oxygen demand. The time variation of DO is formulated as follows:

$$\begin{aligned}\frac{\partial DO}{\partial t} &= \mu_{\max\_X} Phy_x \cdot K_{OC} - m_p Phy_x \cdot K_{OC} - l_{BM} Zoo \cdot K_{OC} \\ &+ k_a \theta_a^{T-20} \left(DO_{sat} - DO\right) - k_{Nh4} \theta_{nh4}^{T-20} NH4 \frac{DO}{K_{nit} + DO} \cdot K_{ON} \\ &- K_{OC} \left(k_{RDOC} \theta_{rdoc}^{T-20} RDOC + k_{LDOC} \theta_{rdoc}^{T-20} LDOC \frac{LDOC}{K_{mLDOC} + LDOC} \right.\end{aligned} \tag{3.32}$$

where, K_{OC} is the oxygen to carbon ratio. K_{ON} is the oxygen to nitrogen ratio. k_a and θ_a^{T-20} denote the reaeration rate at 20°C and the temperature coefficient for reaeration at the sea surface, respectively. k_{Nh4} and θ_{nh4}^{T-20} are the ammonia oxidation rate at 20°C and the temperature coefficient. K_{nit} is the half saturation constant of ammonia oxidation. k_{RDOC} and θ_{rdoc}^{T-20} are the RDOC mineralization rate at 20°C and the temperature coefficient for RDOC mineralization. k_{LDOC} and θ_{Ldoc}^{T-20} mark the LDOC mineralization rate at 20°C and the temperature coefficient for LDOC mineralization. K_{mLDOC} is the half saturation constant for LDOC mineralization. The concentration of DO saturation is proportional to temperature and salinity. Oxygen saturation value is calculated by using the following equation:

$$DO_{Sat} = 14.6244 - 0.36713T + 0.0044972T^2 \\ -0.0966S + 0.00205ST + 0.0002739S^2 \tag{3.33}$$

where T is temperature and S is salinity.

3.1.4 Applications of Models to Nutrients Budget Quantifications

Tokyo Bay is located at the central part of the main island of Japan. The inner bay, the north of which is 50 km in length in its narrowest channel (Fig. 3.7) along the main axis of the bay, connects to the Pacific Ocean. Its average depth and width are 18 m and 25 km, respectively. Tokyo Bay is one of the most eutrophicated bays in Japan. Phytoplankton increase in the surface layer from late spring to early fall, and oxygen depletion and the formation of hydrogen sulfide occur on the sea bed. The sea-water color at the head of the bay sometimes becomes milky blue-green in late summer after a continuous north wind (Koibuchi et al. 2001). This phenomenon is called a blue tide.

In the last decade, a variety of water quality observation equipment has been developed. This has made it easier to measure water quality than in the past. However, even with advanced technology, measuring the flux of nutrients is not easy. To quantify the nutrients budget, we applied our numerical model to Tokyo Bay.

The computational domain was divided into 1km horizontal grids with 20 vertical layers. Computation was carried out from April 1, 1999 to March 31, 2000, with time increments of 300s provided by the Japan Meteorological Agency giving hourly meteorological data that included surface wind stress, precipitation, and solar radiation. At the open boundary, an observed tide level was obtained which can be downloaded from the Japan Oceanographic Data Center (JODC) of the Japan Coastal Guard. DON and DOP was obtained at 30% of TN, TP based on the observation results of Suzumura and Ogawa (2001) at the open boundary.

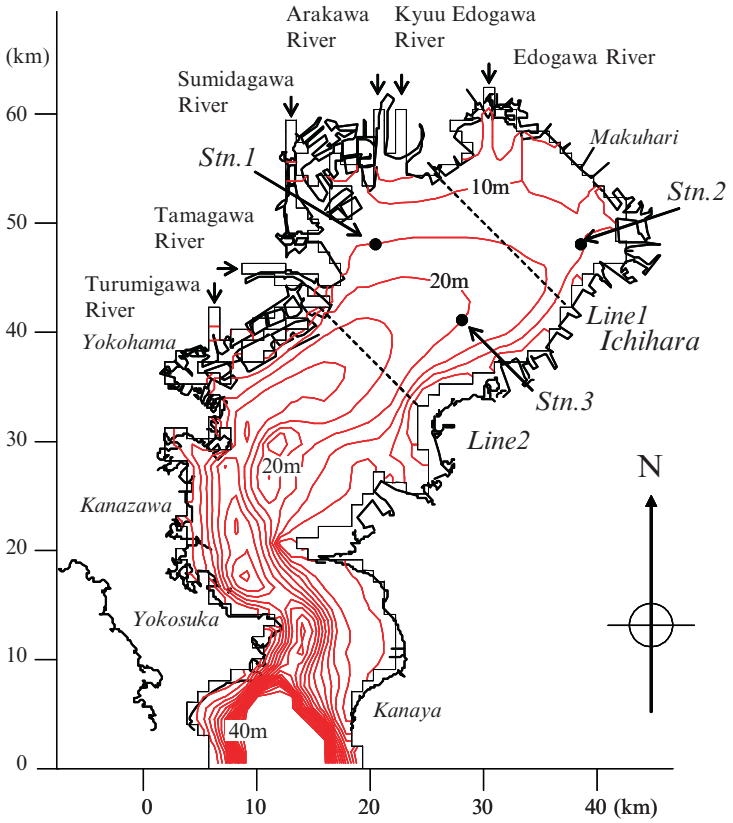

Fig. 3-7. The bathymetry of Tokyo Bay, Japan and its adjacent coastal area, showing the location of measurements in the bay

Fig. 3-8 shows a temporal variation of the computed density at S2. The simulation of water column density over the whole period (April 1999–October 1999) agreed well with measured density. Variations between simulated and observed values were generally less than 0.5 through the water column. Time variation of density effectively reproduced observed results, including short-term wind-induced variation, formation of stratification during summer, and mixing after continuous strong wind in the middle of October. Calculation results also reproduced an upwelling event during the summer season.

Total chlorophyll-a concentrations in the surface water were reproduced relatively well by model simulations. The model captured the temporal increase in chlorophyll-a that were seen in the observation results, as denoted by arrows in Fig. 3-9. During these periods, phytoplankton increased more than 50 μg/l. In Tokyo Bay, a red tide is defined as a chlorophyll *a* concentration of greater than 50μg/l. Four different types of plankton assemblages

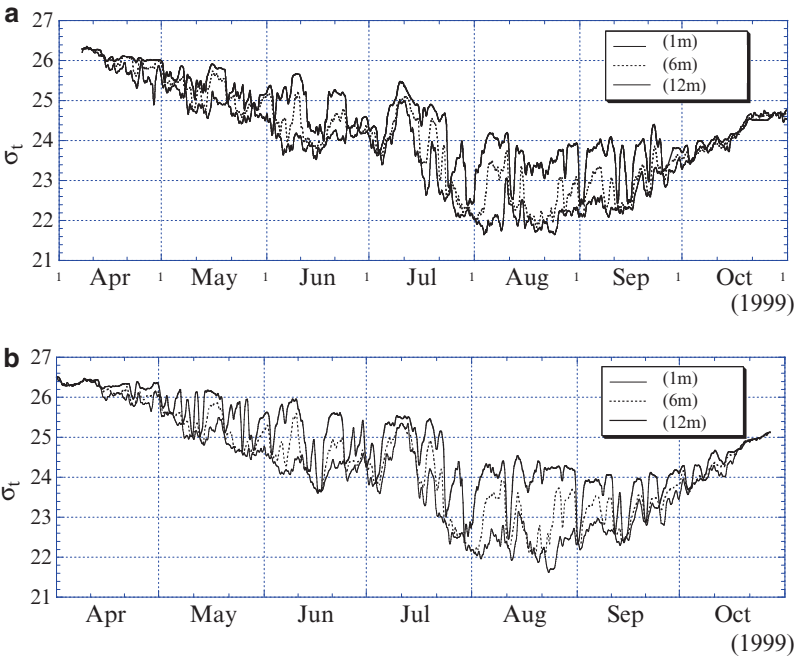

Fig. 3-8. Seasonal cycles of measured (top) and modeled (bottom) density

are defined in this model. This model underestimated the chlorophyll-a concentrations from late September through October.

DO showed high variability compared with field measurements at the bottom, and was relatively higher than the field data from late September through October. Oxygen-depleted water was made on the seabed, representing a basic trend for DO variations (Fig. 3-10).

The simulation of phosphate captured not only the observed increase in the surface layer during the summer season, but also inter-annual variability observed over the study period (Fig. 3-11). For example, phosphate concentrations increased from June to July due to phosphate release from sediment. Simulation results represented this kind of trend based on the oxygen-depleted water.

Fig. 3-12 shows nitrate concentration. Nitrate concentration in the surface layer fluctuated considerably during this period. Nitrate levels doubled or tripled occasionally at the surface. The timing of the high nitrate concentrations and the low density in the surface layer coincided with increases in the river discharge. Concentrations of nitrate were underestimated in bottom waters during summer. Further study is needed to simulate denitrification processes in the sediment layer.

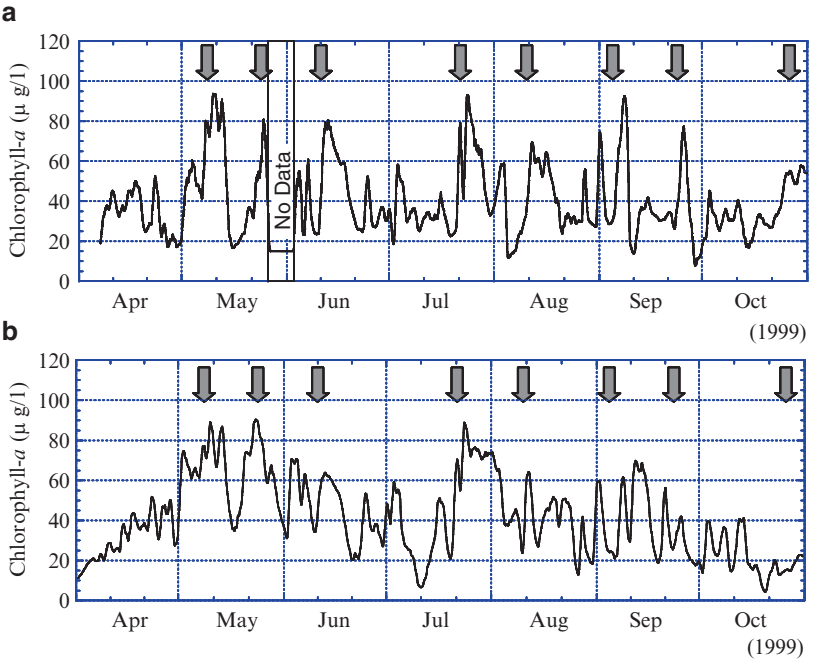

Fig. 3-9. Seasonal cycles of measured chlorophyll-*a* (top) and modeled chlorophyll-*a* (bottom). Arrows denote red tide events (over 50 μg/l)

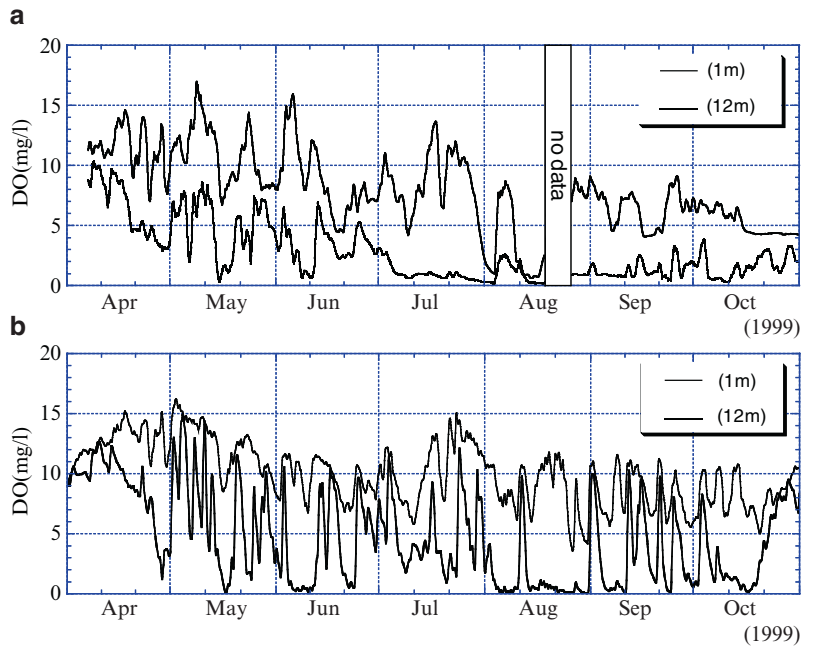

Fig. 3-10. Seasonal cycles of measured DO (top) and modeled DO (bottom) at 1 and 12 m from the sea surface

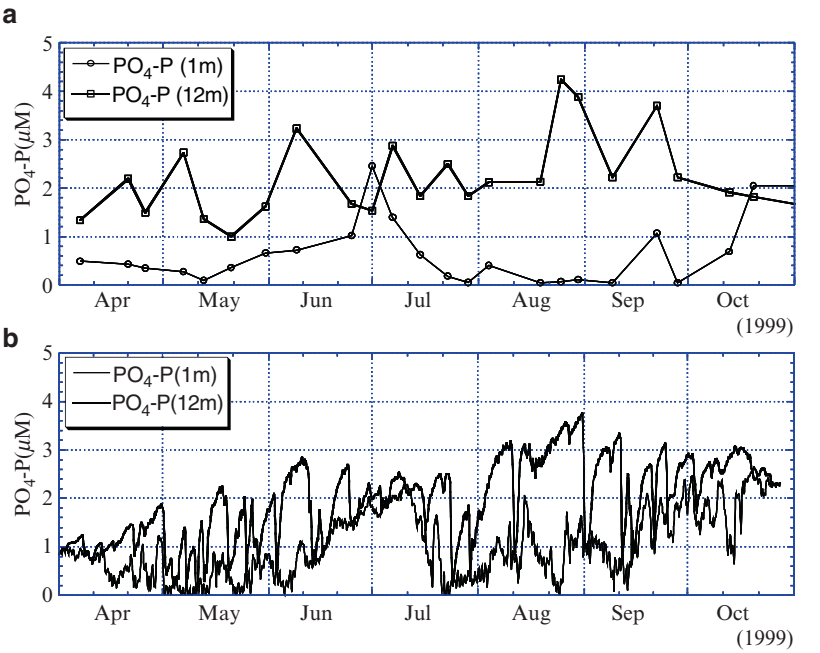

Fig. 3-11. Seasonal cycles of phosphorus measured (top) and modeled (bottom) at 1 and 12 m from the sea surface

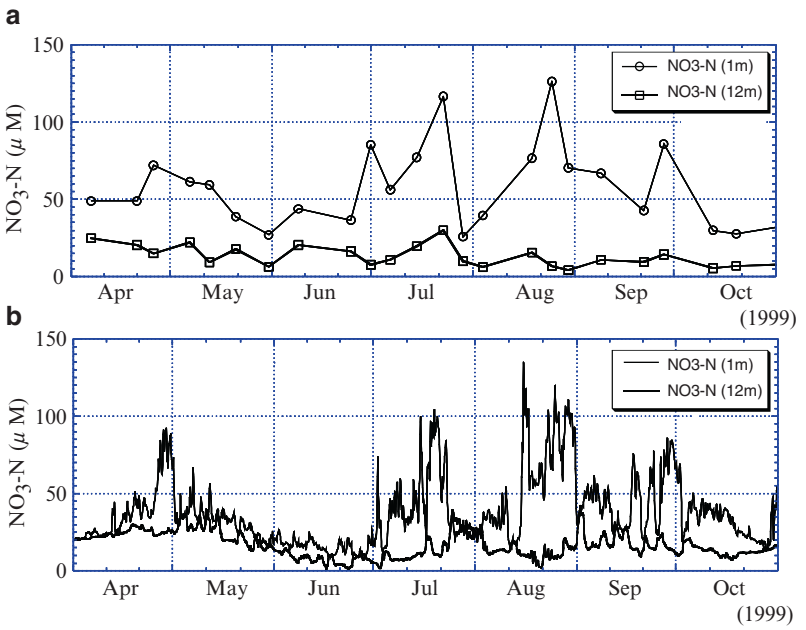

Fig. 3-12. Seasonal cycles of nitrate of measured (top) and modeled (bottom) at 1 and 12 m from the sea surface

Fig. 3-13 shows the calculation results of an annual budget of nitrogen and phosphorus in Tokyo Bay. The annual budget is useful in understanding nutrient cycles. Nitrogen is supplied to a considerable degree from rivers, since atmospheric nitrogen input is significant around urban areas. Phytoplankton uptake the nitrogen and sink to bottom waters, where they are decomposed by heterotrophic processes which consume oxygen. At the head of the bay (between the line 1 and line 2 in Fig. 3-7), about 40% of nitrogen is sunk as detritus and 20% of it is lost into the atmosphere by denitrification. Ammonia released from sediment reaches 20%. About 60% of the nitrogen load flows out from the bay. In contrast, atmospheric phosphorus input to the bay is negligible compared to the contribution of phosphorus from other sources.

Phosphate is released from sediment in the same amount as that discharged from the rivers, and it is transported to the head of the bay by estuarine circulation. As a result, the amount of phosphate in the inner bay remains high. In contrast, nitrogen is mainly supplied from the river mouth and transported quickly out of the bay. In conclusion, nitrogen and phosphorus showed important differences in the mechanisms by which they cycle in

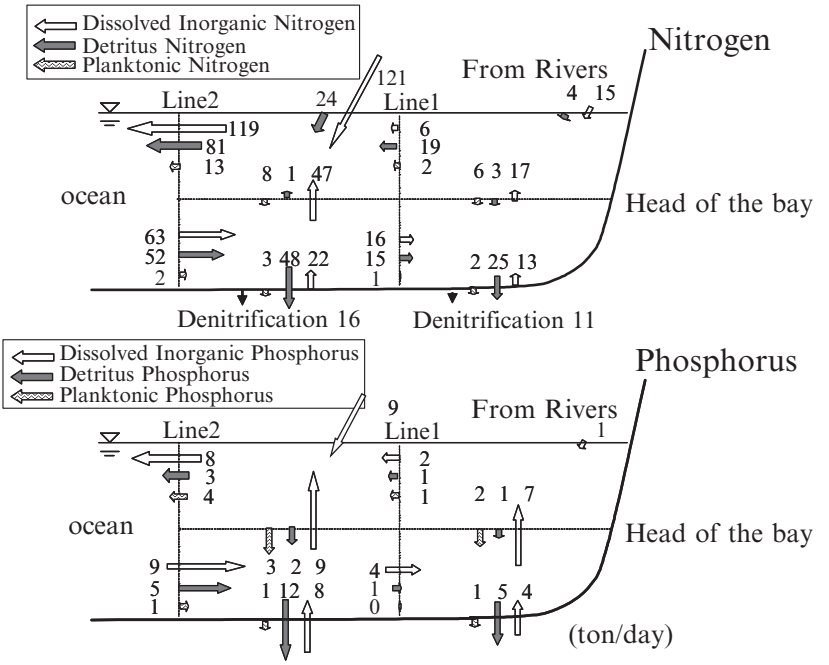

Fig. 3-13. Summary of fluxes and process rates calculated in Tokyo Bay from January 1999 to January 2000. Units are given in ton/year for each element

the bay. The regeneration of nutrients and their release from the sediment is an important source for phytoplankton growth and is equal to the contributions from the rivers. Phosphorus in particular is largely retained within the system through recycling between sediment and water. These results denote the difficulty of improving the eutrophication of bays through the construction of sewage treatment plants alone.

3.2 Application for CSO Modeling

3.2.1 Introduction

Big cities have long been developed near waterfronts. Even now, naval transport remains one of the most important transportation systems, especially for heavy industries and agriculture. Today, many of the world's largest cities are located on coastal zones, and therefore vast quantities of human waste are discharged into near-shore zones (Walker 1990). Fifty percent of the world's populations live within 100 km of the sea. Many people visit urban coastal zones for recreation and leisure, and we also consume seafood harvested from this area. As a result, effluents released into the water pose a risk of pathogen contamination and human disease. This risk is particularly heightened for waters that receive combined sewer overflows (CSOs) from urban cities where both sanitary and storm waters are conveyed in the same sewer system.

To decrease the risk from introduced pathogens, monitoring that is both well designed and routine is essential. However, even though a surprising number of pathogens have been reported in the sea, measuring these pathogens is difficult and time consuming – not least because such pathogens typically exist in a "viable but non-culturable" (VBNC) state.

In addition, the physical environments of urban coastal zones vary widely depending on time and location. Their complicated geographical features border both inland and outer oceans, and so both inland and outer oceans affect them. For example, tidal currents, which are a dominant phenomenon in this area, oscillate according to diurnal periods. Even if the emitted levels of pathogens were constant and we could monitor the levels of pathogen indicator organisms at the same place, they would fluctuate according to tidal periods. Density stratification also changes with the tides.

Consequently, the frequent measurement of pathogens is needed to discuss the risk pathogens pose in urban coastal zones. However, this kind of frequent monitoring appears to be impossible. To solve this conundrum and achieve an assessment of pathogen risk, we developed a set of numerical models that

expand upon the models developed in Sect. 3.1 and that include a pathogens model coupled with a three-dimensional hydrodynamic model.

Section 3.2.2 deals with the distributions of pathogens in urban coastal zones. The pathogens model is explained in greater detail in Sect. 3.2.3. Section 3.2.4 deals with numerical experiments that help to understand the effects of appropriate countermeasures.

3.2.2 Distributions of Pathogens in Urban Coastal Zones

Figure 3-14 shows some typical density distributions patterns in urban coastal zones. The changing balance between tidal amplitudes and river discharge is responsible for the differences among these patterns. As tidal currents increase, the production of turbulent kinetic energy grows and can become the largest source of mixing in the shallow coastal waters. On the other hand, river-discharged water has a low density, creating a density difference between sea water and land-input water.

In salt-wedge estuaries (Fig. 3-14, top), river water is discharged into a small tidal-range sea. The strength of the tidal currents decreases relative to the river flow. This creates a vertical stratification of density. As a result, river water distributes like a veil over the sea's surface and moves seaward.

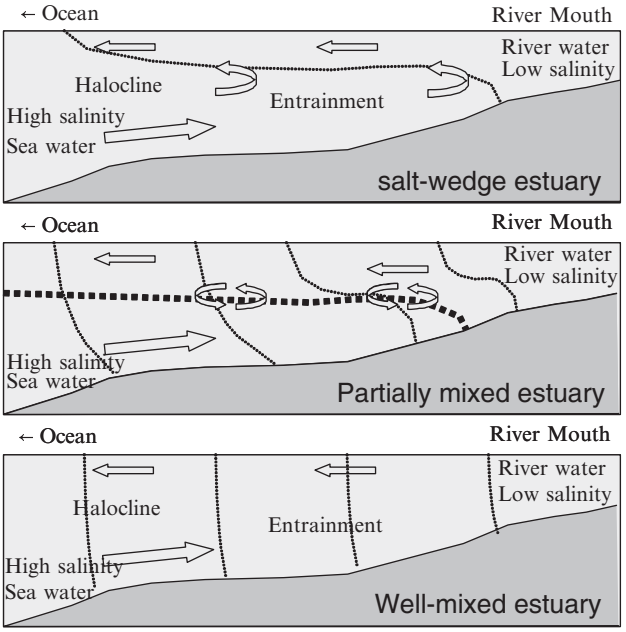

Fig. 3-14. Cross-sectional view of the mixing patterns in urban coastal zones

In contrast, bottom water moves to the river mouth and mixes with the river water. Under such conditions, pathogens move on the surface of the sea, and further mixing with low-density fresh water is restricted by stratification.

In partially mixed estuaries (Fig. 3-14, middle), the tidal force becomes a more effective mixing mechanism. Fresh water and sea water are mixed by turbulent energy. As a result, pathogens that are emitted from sewer treatment plants are more mixed than those in the static salt-wedge estuaries.

In well-mixed estuaries (Fig. 3-14, bottom), the mixing of salt and river waters becomes more complete due to the increased strength of tidal currents relative to river flow. Here, the density difference is developed in a horizontal direction. As a result, pathogens are mixed in the water column and settle down on the sea bed, in turn contaminating estuarine waters during the spring tide or contaminating rainfall through re-suspension (Pommepuy et al. 1992).

Figure 3-15 shows distributions of pathogens under coastal environments. These pathogens encounter a wide range of stresses including UV rays (Sinton et al. 2002), temperature differences (Matsumoto and Omura 1980), pH (Solić and Krstulović 1992), salinity (Omura et al. 1982), and lack of nutrients. The pathogens are transported by currents and continue to become part of sedimentation and to be re-suspended in urban coastal zones (Pommepuy et al. 1992).

3.2.3 Applications of Pathogens Models in Urban Coastal Zones

3.2.3.1 Modeling of Escherichia coliform

The modeling of major pathogens of concern (including Adenovirus, Enterovirus, Rotavirus, Norovirus, and Coronavirus) is not usually conducted owing to the difficulty of modeling and the lack of observational data in coastal environments. We modeled *Escherichia coliform (E. coli)* by using experimental data in coastal sea water.

This model consists of a three-dimensional hydrodynamic model and an *E. coli* model (Onozawa et al. 2005). The mathematical framework employed in the *E. coli* model takes the same approach that was explained in Sect. 3.1.3. The mass balance of *E. coli* is expressed as follows:

$$\frac{\partial Coli}{\partial t}+u_i\frac{\partial Coli}{\partial x_i}+(-Sink)\frac{\partial Coli}{\partial z}=\frac{\partial}{\partial x_i}\left(\varepsilon_i\frac{\partial Coli}{\partial x_i}\right)-sal\cdot Coli \qquad (3.33)$$

where *Coli* denotes concentrations of *E. coli* (CFU/100 ml), and t is time. *Sink* represents the sinking speed of *E. coli*. u_i denotes flow speed for the calculation of the advection term. ε_i denotes the diffusion coefficients. *sal*

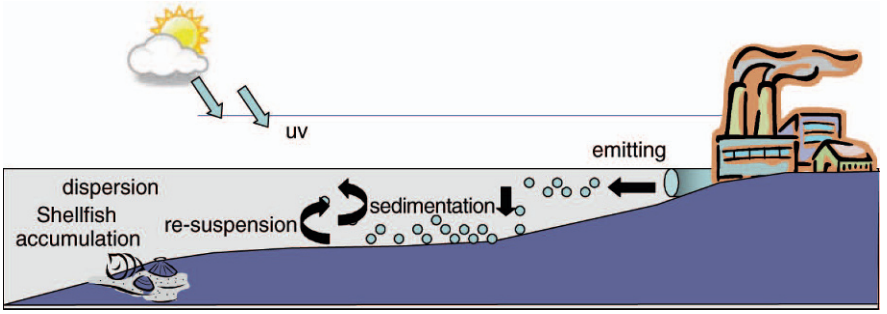

Fig. 3-15. Pathogens transportation in urban coastal zones

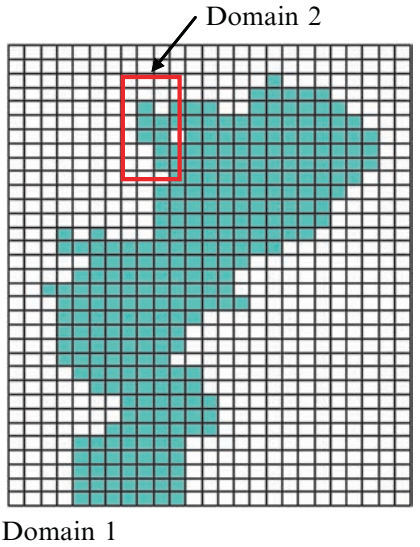

Fig. 3-16. Two nested computational domains

denotes the salinity-dependent die-off rate (ppt/day). Sunlight is generally recognized to be one source by which bacteria are inactivated, due to UV damage to the bacterial cell (Sinton et al. 2002). However, this particular target area has high turbidity that rapidly absorbs UV rays at the sea's surface. As a result, this process has been ignored in this model.

In this model, we can see the numerical simulations performed with two nested domains to fit the complex geography feature around the Odaiba area (Figs. 3-16 and 3-17). These nested grids make possible a representation of the stratification effect. A detailed configuration of the model is summarized in Table 3-2. The two computational domains cover the whole

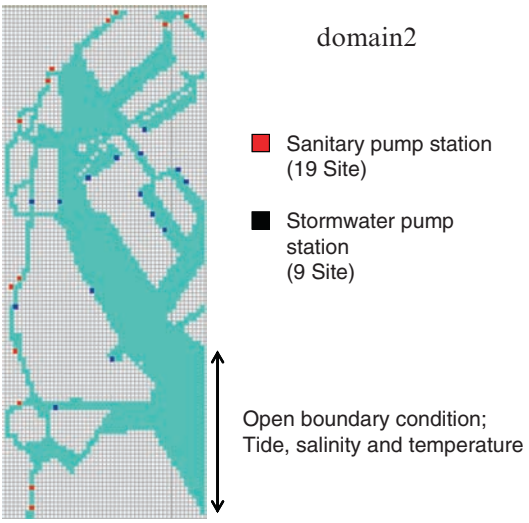

Fig. 3-17. Computational domain 2 and pumping station distributions around the Odaiba area

region of Tokyo Bay and the Odaiba area with grid resolutions of 2 km and 100 m, respectively. The first domain size is 25 × 33 grid points and the second domain has 50 × 127 grid points. All of the domains have 10 vertical sigma levels.

3.2.3.2 Model Validation

Figure 3-18 shows a Tokyo Bay scale grid (domain 1 in Fig. 3-16) that includes both the salinity simulation and observation results. The simulation results show stratification, mixing, and an upwelling phenomenon, and include levels and timing. Fig. 3-19 shows a comparison between observation results and a calculation for temperature and salinity in a fine grid scale (domain 2 in Fig. 3-16). Variations between the simulated and observed values were generally less than 2.5°C and 2 psu through the water column. The timing and periods of upwelling events were captured accurately. After rain fall, river discharge was increased remarkably. Model results adequately represent precipitation variation events and their effects.

Figure 3-20 shows a comparison between modeled and measured *E. coli* at Stn.1. The current standard for acceptably safe beaches for swimming set by of the Ministry of the Environment of Japan is a fecal coliform rate of 1000 coliforms unit per 100 mL (CFU/100 mL). This index of fecal coliform includes not only *E. coli* but also others. However, it is well known that

Table 3-2. Boundary conditions and grid resolution

	Domain 1	**Domain 2**
Computational area	50 km × 66km	5 km × 12.7 km
Grid size (m)	2,000	100
Number of grid	25 × 33 × 10hyer = 8,250	50 × 127 × 10hyer = 63,500
Total number of grid	2,920	22,740
Computational duration	2004/April/1 ~October/31	2004/August/1 ~October/15
Time step	10 min	30 s
Total time step	30,240 step	218,880 step

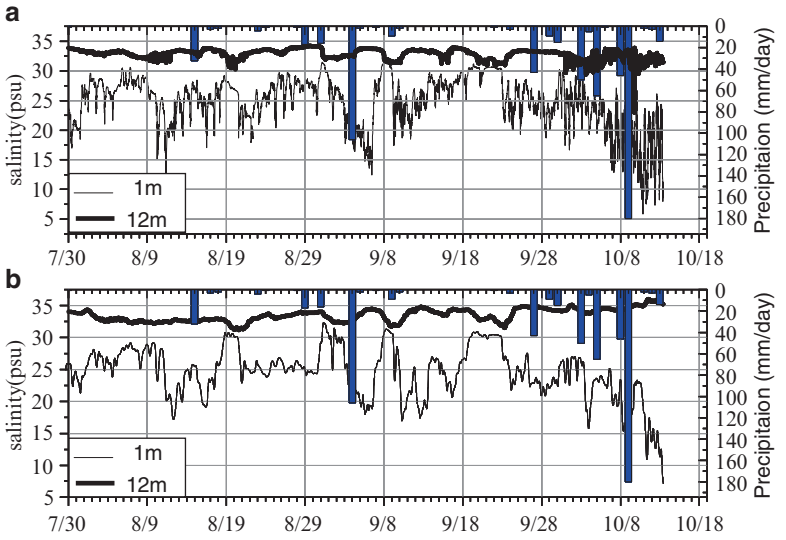

Fig. 3-18. Surface (depth 1 m) and bottom (depth 12 m) salinity derived from observation (**a**) and model simulations (**b**) for the period July 30–October 15

the majority of the fecal coliform in this area comes from *E. coli*. Therefore, we use a value of 1000 CFU/100 ml *E. coli* as the standard for the safety of swimming in the sea. From the calculation results, we can see that durations when the standards are exceeded are very limited, and that most of the summer period falls below the standard for swimming. This result also denotes that the increasing rates of *E. coli* do not agree with levels of precipitation. Even in small precipitations, *E. coli* significantly increased.

Understanding the effects of physical factors is important to understanding the fate and distributions of pathogens. Such an understanding is in turn

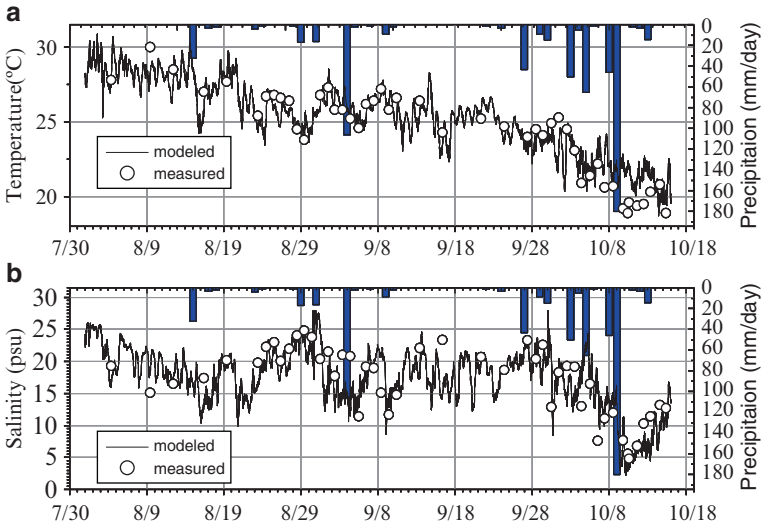

Fig. 3-19. Comparison between measured and modeled temperature (**a**) and salinity (**b**) at Stn.3 with precipitation

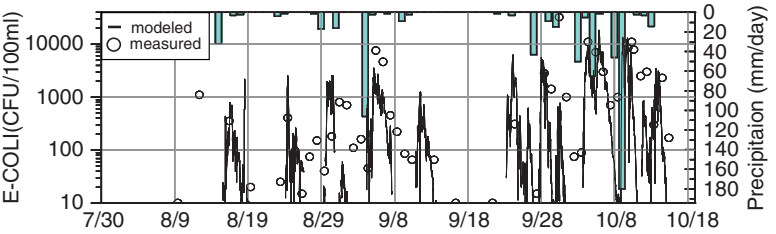

Fig. 3-20. Comparison between measured and modeled *E. coli* at Stn.1

highly related to the assessment of sanitary risks in urban coastal zones. Numerical experiments were thus conducted to examine the variations in rates of *E.coli* according to time and space.

3.2.4 Numerical Experiments with the Pathogens Model in Urban Coastal Zones

3.2.4.1 Numerical Experiments

Variations in levels of *E. coli* are directly correlated with the discharge from pumping stations, tidal currents, river discharges, and density distributions, as explained in Sect. 3.2.2. As a result, the distributions of CSO

differ according to timing, even when the level of discharge is the same. We performed numerical experiments in order to evaluate the contributions of these different discharges and phenomena to CSO distributions. The first numerical experiment was a nowcast simulation that calculated *E. coli* distributions under realistic conditions. The second experiment was a numerical experiment to estimate the effects of a waste-reservoir that was being constructed near the Shibaura area. Numerical experiments were also applied Odaiba area, which is used as a bathing area.

3.2.4.2 Nowcast Simulations of E. coli Distributions

Figure 3-21 shows temporal variations of precipitation and river discharges (top), as well as tide levels and *E. coli* concentrations discharged from three different areas. Shibaura and Sunamachi area are located at the upper bay location from the Odaiba area. Morigasaki has the largest area, but is located in the lower bay location from the Odaiba area (see Fig. 3-17).

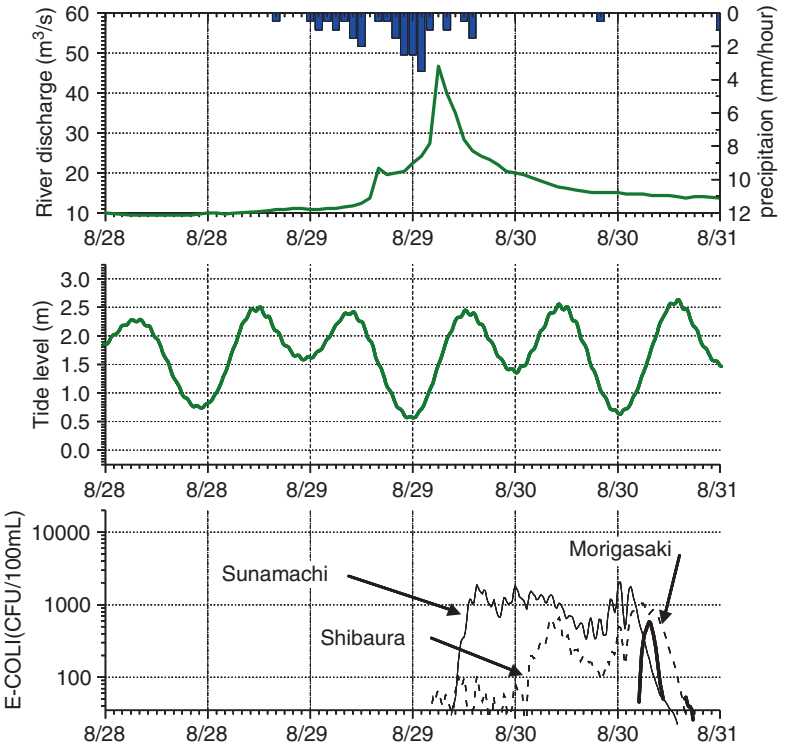

Fig. 3-21. Effect of rainfall and tides for *E. coli* variations under the small precipitation case

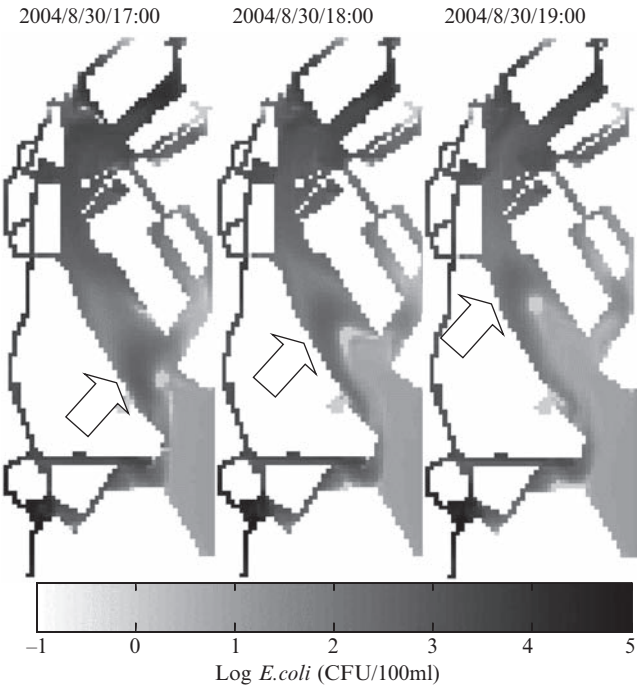

Fig. 3-22. Spatial distributions of *E. coli* at Odaiba area

In this spring tide period, tidal ranges can reach 2 m. Small precipitations were measured from August 29th to 30th. River discharge increased with precipitation, reaching 50 m^3/s. The levels of *E. coli* increased rapidly after the rainfall event, due mainly to discharges from the Sunamachi and Chibaura areas. Near the end of this period of increase, effluent from Morigasaki also reached the Odaiba area. Fig. 3-22 shows the spatial distributions of *E. coli* from three different times. From this Fig., the *E. coli* emitted from the Morigasaki area can be seen to have been transported from the lower region of the bay to the Odaiba area. This is because the small amount of river discharge resulted in a thin layer of low-density, highly concentrated *E. coli* on the surface of the sea, and tended to isolate the *E. coli* by preventing it from mixing with the water column.

In contrast, Fig. 3-23 shows a large precipitation case under the neap tide period. Large amounts of precipitation produced a large river discharge that reached 500 m^3/s. In this period, only the upper bay's CSOs arrived at the Odaiba area. No contributions from the Morigasaki area took place.

In conclusion, the concentrations of *E. coli* vary widely according to space and time. The density distributions produced by the balance of

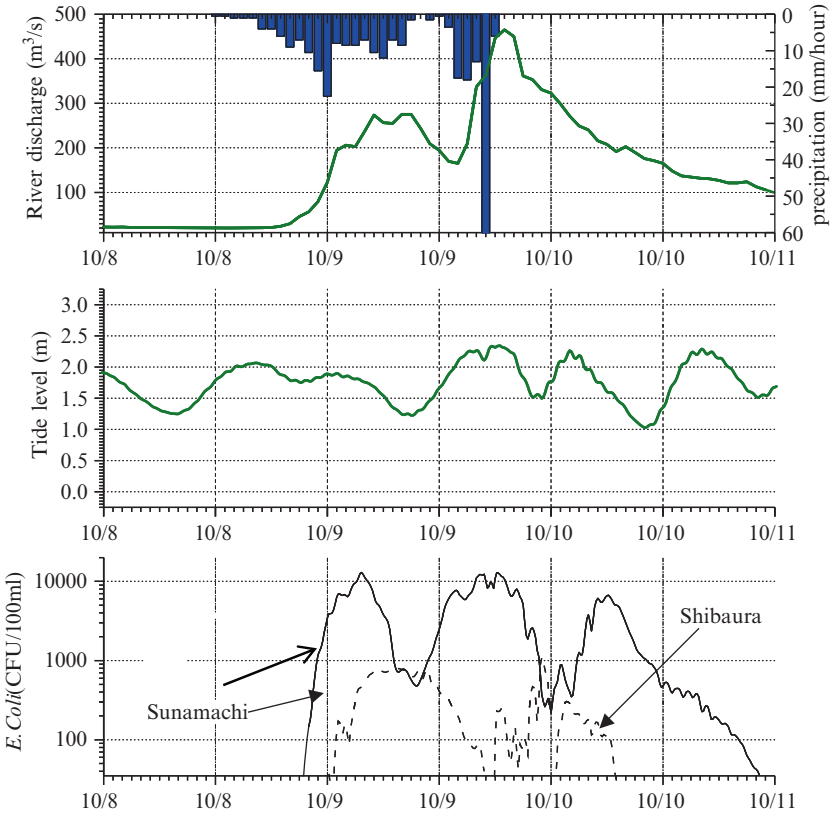

Fig. 3-23. Effect of rainfall and tides for *E. coli* variations under the large precipitation case

tides and river discharges have very complex effects. *E. coli* concentrations reached maximum levels after small precipitation events, but did not increase so much under large precipitation events due to mixing. These kinds of results would be impossible to understand only from observation. The model successfully captured complex distributions of *E. coli* and helped our understanding of pathogens contaminations.

3.2.4.3 Improvement of CSO Systems Through the Construction of Storage Tanks

To mitigate CSO pollutions, the construction of storage tanks at three sites in Tokyo has been planned by the Tokyo Metropolitan Government. Shibaura is the target area of this plan around the Odaiba area. Numerical

Table 3-3. Effects of storage tank

	Stn.l	Stn.2	Stn.3	Stn.4	Stn.5
Before	8.21	2.06	15.44	10.48	3.6
After	6.35	1.96	11.42	8.53	3.31
Improvement	1.86	0.1	4.02	1.95	0.29

Unit: day

experiments were conducted to evaluate the effects of storage tanks on CSOs. Calculation results were compared by the duration of periods when the amount of CSOs in the Odaiba area exceeded bathing standards.

Numerical simulation was performed with and without the proposed storage tank, which has a capacity of 30,000 m^3. This storage tank can store CSOs after rainfall. To include the effect of continuous rain, we assumed that the CSOs stored in the tank could be purified within 1 day.

Table 3.3 shows the calculation results for the mitigation effect of the storage tank. These numbers denote the dates when the standards for bathing in the sea (over 1000 CFU/100 ml) were exceeded. Fig. 3.17 shows the observation stations. From this table, Stn.3 shows the largest decrease in CSOs among these five stations. This is because Stn.3 is located closest to the pumping stations, and therefore would be most sensitive to the CSOs. Before the construction of the CSO storage tank, minimum bathing standards for CSO levels were exceeded on 15 days. After the construction of the storage tank, the duration of CSO levels that exceeded safety standards decreased to 11 days. There was an improvement of 4 days. On the other hand, other stations only 2 days, or in some cases, less than 1 day. Such differences could not be observed, especially in those stations that are located inside the Odaiba area due to the enclosed feature of bathymetry.

For example, over 10,000 storage tanks have been built in Germany alone, and another 10,000 were planned during the 1980s in Germany. Our plans for dealing with CSOs are not enough to mitigate the effects of CSOs completely. At the same time, these results show us the complexity of pathogens distributions and the importance of numerical modeling for this problem.

3.2.5 Summary

Numerical simulation is one of the most important tools for the management of water quality and ecosystems in urban coastal zones. We have developed a water quality model to simulate both nutrient cycles and pathogens distributions, and coupled it with a three-dimensional hydrodynamic model of urban

coastal areas. To quantify the nutrients budget, a numerical model should include material cycles with phytoplankton, zooplankton, carbons, nutrients, and oxygen. We applied this model to the Tokyo Bay and simulated water column temperatures, salinity, and nutrient concentrations that were closely linked with field observations. This model successfully captured periods of timing, stratification events, and subsequent changes in bottom water oxygen and nutrients. Our model results also indicated that there were clear differences between the material cycles of nitrogen and phosphorus inside the bay. The regeneration of nutrients and its release from sediment was found to be a source of phytoplankton growth on the same order of importance as contributions from rivers. In particular, phosphorus was found to have been largely retained within the system through recycling between sediment and water.

We also developed a pathogen model that includes *E. coli* and is applied to the simulation of CSO influences in urban coastal zones. These results indicate that, because of stratification, concentrations of *E. coli* significantly increase after even small precipitation events. From this study, the balance between tidal mixing and river waters can be seen to be significant. However, these are only two case studies; it remains necessary to simulate the structure and characteristics of CSO distributions and their impact on urban coastal zone pollution. Such simulations remain as future works to be undertaken.

References

Ærtebjerg G, Andersen JH, Hansen OS (2003) Nutrients and Eutrophication in Danish Marine Waters, Vol. Ministry of the Environment, National Environmental Research Institute

Blumberg AF, Mellor GL (1987) A description of a three-dimensional coastal ocean circulation model, Vol. American Geophysical Union, Washington, DC.

Caperon J, Cattel SA, Krasnick G (1971) Phytoplankton kinetics in a subtrophical estuary: eutrophication. Limnol Oceanogr 16:599–607

Cerco CF, Cole T (1993) Three-dimensional eutrophication model of Chesapeake Bay. J Environ Eng 119:1006–1025

Cerco CF, Cole T (1995) User's guide to the CE-QUAL-ICM: three-dimensional eutrophication model, Vol. Vicksburg, MS

Chai F, Dugdale RC, Peng TH, Wilkerson FP, Barber RT (2002) One Dimensional Ecosystem Model of the Equatorial Pacific Upwelling System Part I: Model Development and Silicon and Nitrogen Cycle. Deep-Sea Res II 49:2713–2745

Eppley RW (1972) Temperature and phytoplankton growth in the sea. Fish Bull 70:1063–1085

Evans GT, Parslow JS (1985) A model of annual plankton cycles. Biol Oceanogr 3:327–347

Fasham MJR, Ducklow HW, Mckelvie SM (1990) A nitrogen-based model of phytoplankton dynamics in the oceanic mixed layer. J Mar Res 48:591–639

Fitzgerald GP, Nelson TC (1966) Extractive and enzymatic analysis for limiting or surplus phosphorus in algae. J Phycol 2:32–37

Freeman NG, Hale AM, Danard MB (1972) A modified sigma equations; approach to the numerical modeling of great lake hydrodynamics. J Geophys Res 77: 1050–1060

Haidvogel DB, Arango HG, Hedstrom K, Beckmann A, Rizzoli PM, Shchepetkin AF (2000) Model evaluation experiments in the North Atlantic Basin: simulations in nonlinear terrain-following coordinates. Dyn. Atmos. Oceans 32:239–281

Hydroqual (2004) User's guide for RCA, Release 3.0., Hydroqual, Inc., NJ

Jøgensen BB, Richardson K (1996) Eutrophication in Coastal Marine Ecosystem, vol 52. American Geophysical Union, Washinton DC

Johnson BH, Kim KW, Heath RE, Hseish NN, Butler HL (1993) Verification of a three-dimensional hydrodynamic model of Chesapeake Bay. J Hydraul Eng 119:2–20

Kantha LH, Clayson CA (2000) Small Scale Processes in Geophysical Fluid Flows, Academic Press. 888pp

Kishi MJ, Kashiwai M, Wared DM, Megreye BA, Eslingerf DL, Wernerg FE, Maki Noguchi-Aitab TA, Masahiko Fujii j w, Shinji Hashimotok, Daji Huangl, Hitoshi Iizumim, Yukimasa Ishidav, Sukyung Kango GAK, Hyun-cheol Kimo, Kosei Komatsun, Vadim V. Navrotskyq SLS, Kazuaki Tadokorob,x, Atsushi Tsudam,r, Orio Yamamuram YY, b, Katsumi Yokouchis, Naoki Yoshiei,v, Jing Zhangt YIZ, Vladimir I. Zvalinskyq (2007) NEMURO – a lower trophic level model for the North Pacific marine ecosystem. Ecol Modell 202:12–25

Koibuchi Y, Isobe M (2005) Blue Tide occurred in the west of Tokyo Bay in Summer of 2004. Proceeding 3rd international conference on Asia and Pacific Coast 1512-1521

Koibuchi Y, Sasaki J, Isobe M (2001) Study on Budget and Circulation of Nitrogen and Phosphorus in Tokyo Bay. Proc Coast Eng 48:1076–1080

Kremer JN, Nixon SW (1978) A coastal marine ecosystem: simulation and analysis, vol 24. Springer, Heidelberg

Li M, Zhong L, Boicourt WC (2005) Simulations of Chesapeake Bay estuary: sensitivity to turbulence mixing parameterizations and comparison with observations. J Geophys Res 110:C12004. doi: 10.1029/2004JC002585

Lucas LV, Koseff JR, Colern JE, Monismith SG, Thompson JK (1999) Processes governing phytoplankton blooms in estuaries. II. The role of transport in global dynamics. Mar Ecol Prog Ser 187:17–30

MacCready P, Hetland RD, Geyer WR (2002) Long-term isohaline salt balance in an estuary. Cont Shelf Res 22:1591–1601

Matsukawa YKS (1990) Nitrogen budget in Tokyo Bay with special reference to the low sedimentation to supply ratio. J Oceanogr 46:44–54

Matsumoto J, Omura T (1980) Some factors affecting the survival of fecal indicator bacteria in sea water. Technol Rep 45:169–185

Mellor GL (1973) Analytic prediction of the properties of stratified planetary surface layers. J Atmos Sci 30:1061–1069

Mellor GL, Yamada T (1982) Development of a turbulence closure model for geophysical fluid problems. Rev Geophys 20:851–875

Omura T, Onuma M, Hashimoto Y (1982) Viability and adaptability of E-COLI. and Enterococcus group to salt water with high concentration of sodium chloride. Wat Sci Tech 14:115–126

Onozawa K, Koibuchik Y, Furumai H, Katayama H, Isobe M (2005) Numerical calculation of combined sewer overflow(CSO) due to heavy rain around Daiba in the head of Tokyo Bay. Annu J Coast Eng 52:891–895

Pett R (1989) Kenetics of microbial mineralization of organic carbon from detrital *Skeletonema costatum* cells. Mar Ecol Prog Ser 52:123–128

Phillips NA (1957) A coordinate system having some special advantages for numerical forecasting. J Meteorol 14:184–185

Pommepuy M, Guillaud JF, Dupray E, Derrien A, Le Guyader F, Cormier M (1992) Enteric bacterial survival factors. Water Sci Technol 25:93–103

Prudman J (1953) Dynamical oceanography, Vol. Methuen & Co, London

Sinton LW, Hall CH, Lynch PA, Davies-Colley RJ (2002) Sunlight inactication of fecal indicator bacteria and bacteriophages from waste stabilization pond effluent in fresh and saline waters. Appl Environ Microbiol 68:1122–1131

Solić M, Krstulović N (1992) Separate and combined effects of solar radiation, temperature, salinity, and pH on the survival of feacal coliforms in seawater. Mar Pollut Bull 24:411–416

Suzumura M, Ishikawa K, Ogawa H (1998) Characterization of dissolved organic phosphrous in coastal seawater using ultrafiltration and phosphoydrolytic enzymes. Limnology and Oceanography 43:1553–1564

Unoki S (1998) Relation between the Transport of Gravitational Circulation and the River Discharge in Bays. J Oceanogr 7:283–292

Waite A, Bienfang PK, Harrison PJ (1992) Spring bloom sedimentation in a subarctic ecosystem. Mar Biol 114:131–138

Walker HJ (1990) The coastal zone. In the Earth as Transformed by Human Action. Local and Regional Changes in the Biosphere over the Past 300 Years, Vol. Cambridge University Press, Cambridge

Yamaguchi Y, Satoh H, Aruga Y (1991) Seasonal changes of organic carbon and nitrogen production by phytoplankton in the estuary of River Tamagawa. Mar Pollut Bull 23:723–725